The Astrophysical Journal Supplement Series, 200:17 (16pp), 2012 June doi:10.1088/0067-0049/200/2/17

THE CHANDRA MULTI-WAVELENGTH PROJECT: OPTICAL SPECTROSCOPY AND THE BROADBAND SPECTRAL ENERGY DISTRIBUTIONS OF X-RAY-SELECTED AGNs

Markos Trichas[1], Paul J. Green[1], John D. Silverman[2], Tom Aldcroft[1], Wayne Barkhouse[3], Robert A. Cameron[4], Anca Constantin[5], Sara L. Ellison[6], Craig Foltz[7], Daryl Haggard[8], Buell T. Jannuzi[9], Dong-Woo Kim[1], Herman L. Marshall[10], Amy Mossman[1], Laura M. Pérez[11], Encarni Romero-Colmenero[12], Angel Ruiz[13], Malcolm G. Smith[14], Paul S. Smith[15], Guillermo Torres[1], Daniel R. Wik[16], Belinda J. Wilkes[1], and Angie Wolfgang[17]
[1] Harvard-Smithsonian Center for Astrophysics, Cambridge, MA 02138, USA; mtrichas@cfa.harvard.edu
[2] Institute for the Physics and Mathematics of the Universe (IPMU), University of Tokyo, Kashiwanoha 5-1-5, Kashiwa-shi, Chiba 277-8568, Japan
[3] Department of Physics and Astrophysics, University of North Dakota, Grand Forks, ND 58202, USA
[4] W. W. Hansen Experimental Physics Laboratory, Kavli Institute for Particle Astrophysics and Cosmology, Department of Physics and SLAC National Accelerator Laboratory, Stanford University, Stanford, CA 94305, USA
[5] Department of Physics and Astronomy, James Madison University, PHCH, Harrisonburg, VA 22807, USA
[6] Department of Physics and Astronomy, University of Victoria, Victoria, BC V8P 1A1, Canada
[7] Division of Astronomical Sciences, National Science Foundation, 4201 Wilson Blvd., Arlington, VA 22230, USA
[8] Center for Interdisciplinary Exploration and Research in Astrophysics, Northwestern University, 2145 Sheridan Road, Evanston, IL 60208, USA
[9] NOAO, Kitt Peak National Observatory, Tucson, AZ 85726, USA
[10] Kavli Institute for Astrophysics and Space Research, Massachusetts Institute of Technology, 77 Massachusetts Ave., Cambridge, MA 02139, USA
[11] Department of Astronomy, California Institute of Technology, 1200 East California Blvd, Pasadena, CA 91125, USA
[12] South African Astronomical Observatory, P.O. Box 9, Observatory, 7935, South Africa
[13] Osservatorio Astronomico di Brera–INAF, Milan, Italy
[14] Cerro Tololo Interamerican Observatory, La Serena, Chile
[15] Steward Observatory, University of Arizona, 933 Cherry Ave., Tucson, AZ 85721, USA
[16] NASA Goddard Space Flight Center, Greenbelt, MD 20771, USA
[17] Department of Astronomy and Astrophysics, University of California, Santa Cruz, CA 95064, USA
Received 2011 December 23; accepted 2012 April 21; published 2012 May 30

ABSTRACT

From optical spectroscopy of X-ray sources observed as part of the Chandra Multi-wavelength Project (ChaMP), we present redshifts and classifications for a total of 1569 *Chandra* sources from our targeted spectroscopic follow-up using the FLWO/1.5 m, SAAO/1.9 m, WIYN 3.5 m, CTIO/4 m, KPNO/4 m, Magellan/6.5 m, MMT/6.5 m, and Gemini/8 m telescopes, and from archival Sloan Digital Sky Survey (SDSS) spectroscopy. We classify the optical counterparts as 50% broad-line active galactic nuclei (AGNs), 16% emission line galaxies, 14% absorption line galaxies, and 20% stars. We detect QSOs out to $z \sim 5.5$ and galaxies out to $z \sim 3$. We have compiled extensive photometry, including X-ray (ChaMP), ultraviolet (*GALEX*), optical (SDSS and ChaMP-NOAO/MOSAIC follow-up), near-infrared (UKIDSS, Two Micron All Sky Survey, and ChaMP-CTIO/ISPI follow-up), mid-infrared (*WISE*), and radio (FIRST and NVSS) bands. Together with our spectroscopic information, this enables us to derive detailed spectral energy distributions (SEDs) for our extragalactic sources. We fit a variety of template SEDs to determine bolometric luminosities, and to constrain AGNs and starburst components where both are present. While ∼58% of X-ray Seyferts ($10^{42}\,\mathrm{erg\,s^{-1}} < L_{2-10\,\mathrm{keV}} < 10^{44}$ erg s^{-1}) require a starburst event (>5% starburst contribution to bolometric luminosity) to fit observed photometry only 26% of the X-ray QSO ($L_{2-10\,\mathrm{keV}} > 10^{44}$ erg s^{-1}) population appear to have some kind of star formation contribution. This is significantly lower than for the Seyferts, especially if we take into account torus contamination at $z > 1$ where the majority of our X-ray QSOs lie. In addition, we observe a rapid drop of the percentage of starburst contribution as X-ray luminosity increases. This is consistent with the quenching of star formation by powerful QSOs, as predicted by the merger model, or with a time lag between the peak of star formation and QSO activity. We have tested the hypothesis that there should be a strong connection between X-ray obscuration and star formation but we do not find any association between X-ray column density and star formation rate both in the general population or the star-forming X-ray Seyferts. Our large compilation also allows us to report here the identification of 81 X-ray Bright Optically inactive Galaxies, 78 $z > 3$ X-ray sources, and eight Type-2 QSO candidates. Also, we have identified the highest redshift ($z = 5.4135$) X-ray-selected QSO with optical spectroscopy.

Key words: galaxies: evolution – galaxies: Seyfert – galaxies: starburst – quasars: general – techniques: spectroscopic – X-rays: galaxies

Online-only material: color figures

1. INTRODUCTION

Our understanding of how galaxies form and evolve has significantly advanced in the last few years. Large spectroscopic programs (e.g., 2dFGRS, Sloan Digital Sky Survey (SDSS), and DEEP2) have shown that the evolution of galaxies strongly depends on their position in the cosmic web. A striking manifestation of this link is the suppression of the star formation in increasingly dense environments (e.g., Kauffmann et al. 2004; Cooper et al. 2006; Netzer 2009; Schawinski et al. 2009). In addition, there is now strong evidence that powerful active galactic nuclei (AGNs) play a key role in the evolution of galaxies. The correlation of central black hole and stellar bulge mass (M_{BH}-σ; e.g., Magorrian et al. 1998), and the similarity between the cosmic star formation history (e.g., Hopkins & Beacom 2006) and cosmic black hole mass assembly history

(e.g., Aird et al. 2010) in massive galaxies, both suggest that the growth of supermassive black holes (SMBHs) is related to the growth of host galaxies. The apparently independent observational trends above are believed to hold the key to galaxy assembly, but the detailed physical mechanism(s) behind them remain poorly understood. For example, although processes like galaxy suffocation, harassment, and ram-pressure stripping are proposed to explain the star formation/density relation (e.g., Haines et al. 2006), they usually operate in rich and hence rare environments (i.e., massive clusters). The vast majority of galaxies inhabit less dense regions (poor clusters, groups, and field), where alternative mechanisms should dominate. Understanding what drives the formation and evolution of galaxies and their central SMBHs remains one of the most significant challenges in extragalactic astrophysics.

Recent attention has focused on models where AGN feedback regulates the star formation in the host galaxy. These scenarios are consistent with the $M_{\rm BH}$–σ relation and make various predictions for AGN properties, including the environmental dependence of the AGN/galaxy interplay and the relative timing of periods of peak star formation and nuclear accretion activity. The key feature of these models is that they can potentially link the apparently independent observed relations between star formation, AGN activity, and large-scale structure to the same underlying physical process. For example, in the "radio-mode" model of Croton et al. (2006), accretion of gas from cooling flows in dense environments (e.g., group and cluster) may produce relatively low-luminosity AGNs, which in turn heat the bulk of the cooling gas and prevent it from falling into the galaxy center to form stars. Alternatively, Hopkins et al. (2006) propose that mergers trigger luminous QSOs and circumnuclear starbursts, which both feed and obscure the central engine for most of its active lifetime. In this scenario, AGN outflows eventually sweep away the dust and gas clouds, thereby quenching the star formation. This "QSO-mode" likely dominates in poor environments (e.g., field and group), as the high-velocity encounters, common in dense regions, do not favor mergers. These proposed models make clear, testable predictions about the properties of AGNs, while observational constraints provide first-order confirmation of this theoretical picture (e.g., Lehmer et al. 2009). Merger-driven scenarios, for example, predict an association between optical morphological disturbances, star formation, and an intense obscured AGN phase in low-density regions. The "radio-mode" model, in contrast, invokes milder AGN activity in early-type hosts and relatively dense environments with little or no star formation.

While it is now recognized that black holes play a fundamental role in shaping the galaxy population, the sequence in which galaxies build up their stellar and black hole mass and the relationship between the two components are, as yet, poorly understood. In some models (e.g., Di Matteo et al. 2005; Hopkins et al. 2006) the stellar population and the SMBHs form almost simultaneously and therefore predict a correlation between star formation and AGN activity. Contrary to that scenario, it is also proposed that the stellar population of galaxies is accumulated first, followed by the main epoch of SMBH growth (e.g., Archibald et al. 2002; Cen 2011). In the latter class of models, one expects star formation and AGN activity to be unrelated, or even negatively correlated. A major complexity in addressing this question observationally is assessing the level of star formation in AGNs. Particularly at $z > 1$, the main epoch of galaxy and SMBH formation, it is difficult to decompose the stellar from the AGN emission, especially in the case of dust enshrouded systems. When they are accreting rapidly, AGNs can dominate the radiation from stars over almost the entire electromagnetic spectrum. There are, however, two key energy ranges that allow the most effective separation between the radiation from accretion and from star formation. The X-ray band provides a clean window in which the radiation from luminous AGNs ($L_X(2\text{–}10\,\mathrm{keV}) > 10^{42}\,\mathrm{erg\,s^{-1}}$) can be observed with minimal contamination from star formation, while star-forming galaxies emit a large fraction of their energy in the infrared band where the AGN contribution is minimal. Combining X-ray with longer wavelength data and optical spectroscopy can provide a handle on this issue (e.g., Trichas et al. 2009, 2010; Kalfountzou et al. 2011; Civano et al. 2012). X-ray surveys have proved to be by far the most efficient way of finding AGNs, and in relatively shallow surveys, AGNs will completely dominate the source population. When a hard bandpass is available (>2 keV), as with *Chandra*, one can detect X-ray AGNs that might otherwise be completely missed in other surveys due to obscuration. However, lack of observational data limits the information on the interplay between AGNs, star formation, and local density, particularly at $z > 1$, close to the peak of the AGN and star formation activity of the universe (e.g., Barger et al. 2005). Addressing these key questions requires the identification of large numbers of AGNs at $z > 1$ over a broad range of environments for which a precise estimation of their bolometric luminosity will allow us to determine the relative contribution of AGNs and star formation to the bolometric emission.

The above questions have motivated efforts to study the multi-wavelength properties of AGNs combining data from various space- and ground-based telescopes. The *Chandra* and *XMM-Newton* Observatories are, for the first time, resolving the hard (2–10 keV) Cosmic X-ray Background (CXRB) into individual sources. Based on the spectral shape of the CXRB, the majority of emission from accretion powered sources has been obscured from our view. While unabsorbed AGNs dominate the soft (0.1–2 keV) CXRB (Hasinger et al. 1998), the high-energy CXRB spectrum (2–30 keV) is harder than that of known AGNs (Gilli & Hasinger 2001). With recent *Chandra* observations of the Chandra Deep Field North (Brandt et al. 2001), South (Rosati et al. 2002), and *XMM-Newton* observations of the Lockman Hole (Hasinger et al. 2001), ∼75% of the hard (2–8 keV) XRB has been resolved into point sources. The resolved fraction decreases with increasing X-ray energy (Worsley et al. 2006), but approaches 80%, e.g., when X-rays at the position of faint optical sources are stacked (Hickox & Markevitch 2006). Many of the hardest serendipitous sources found so far arise in otherwise unremarkable bright galaxies (Hornschemeier et al. 2001; Tozzi et al. 2001), which may contain very heavily obscured AGNs. In addition, *Chandra* has begun to detect the extremely rare, heavily obscured, and dust enshrouded quasars (Norman & Impey 2001; Stern et al. 2002). Wider area surveys are needed to study these X-ray emitting populations with significant statistics. The Chandra Multi-wavelength Project (ChaMP) is a medium depth, wide*area sample of serendipitous X-ray sources from archival *Chandra* fields. ChaMP effectively bridges the gap between flux limits attained by past large-area X-ray surveys and recent Chandra Deep Fields. The complete project has detected a total of >19,000 X-ray sources (Green et al. 2009) over 33 deg^2 with >9000 X-ray sources positionally matched to SDSS optical sources (Kim et al. 2007). However, to fully study the properties of X-ray-detected AGNs, good quality spectra are needed for redshifts, luminosities, and source classification.

In this paper, we describe the large sample of optical spectroscopy available for our ChaMP sources with a suite of available multi-wavelength data ranging from X-rays to radio. These data are used to test the predictions of the different feedback models proposed to explain the apparent relationship between AGNs and star formation activity. In Section 2, we describe our optical spectroscopy and ancillary multi-wavelength data. Section 3 summarizes the template fitting method used to produce spectral energy distributions (SEDs) for all our extragalactic objects, while Sections 4 and 5 describe the X-ray spectral fitting, star formation rates (SFRs), and black hole mass estimates. Sections 6–8 discuss what our observations suggest regarding the different feedback models, while Sections 9 and 10 briefly summarize the interesting populations of X-ray Bright Optically inactive Galaxies (XBONGs) and high-redshift objects found within our sample. Section 11 is a summary of our findings. A cosmological model with $\Omega_o = 0.3$, $\lambda_o = 0.7$, and a Hubble constant of 72 km s^{-1} Mpc^{-1} is used throughout.

2. CHAMP OBSERVATIONS

2.1. Imaging

The ChaMP is a wide-area serendipitous X-ray survey based on archival X-ray images of the ($|b| > 20$ deg) sky observed with the AXAF CCD Imaging Spectrometer onboard *Chandra*. The ChaMP covers a total of 392 fields, omitting pointings from dedicated serendipitous surveys like the Chandra Deep Fields as well as fields with large bright optical or X-ray sources. The list of *Chandra* pointings avoids any overlapping observations by eliminating the observation with the shorter exposure time. As described in Green et al. (2004), we also avoid fields with extended sources ($>3'$) in either optical or X-rays. Spurious X-ray sources have been flagged and removed as described in Kim et al. (2007). Of the 392 ChaMP ObsIDs, which average 0.1 deg^2 sky area each, at the brightest fluxes, 323 overlap with the SDSS (DR5) footprint (Covey et al. 2008; Green et al. 2009; Haggard et al. 2010).

Optical imaging provides optical fluxes, preliminary source classification, and accurate centroiding for spectroscopic follow-up. As a result, the ChaMP team supplemented observed *Chandra* imaging with deep optical observations (Green et al. 2004). ChaMP fields were observed with NOAO 4 m imaging with the Mosaic CCD cameras (Muller et al. 1998), which provided adequate depth, spatial resolution ($\sim 0\farcs6$ pixel^{-1}), and a large field of view ($36' \times 36'$) over the full *Chandra* field of view. NOAO filters similar to SDSS g', r', and i' passbands were used for 66 such fields, reaching down to AB magnitudes of 26.1, 25.4, and 24.4, respectively (Green et al. 2004). The positional uncertainty of ChaMP X-ray source centroids has been analyzed via X-ray simulations by Kim et al. (2007). An automated matching procedure between each optical position and the ChaMPs X-ray source catalog was first performed with ~95% of the matched sample having an X-ray/optical position difference of $<3''$ yielding a sample of 1376 unique matches. In addition to the automated matching procedure, we also performed visual inspection of both X-ray and optical images, overplotting the centroids and their associated position errors retaining the highest confidence matches (Green et al. 2009).

2.2. Optical Spectroscopy

The spectroscopic follow-up of *Chandra* sources operated in three modes based on optical magnitude. Spectra for the brightest sources ($r < 17$) are obtained primarily with the FLWO/1.5 m FAST spectrograph and the SAAO/1.9 m grating spectrograph. For most sources with $17 < r < 21$, we used the WIYN and the CTIO/4 m with HYDRA, a multi-fiber spectrograph. To obtain spectra for the faint source population ($r > 21$), slit and multi-object spectroscopy with a 4–8 m class telescope is required (i.e., KPNO/4 m, MMT, Magellan, and Gemini). In total, 22 nights of WIYN/Hydra (multi-fiber) time, 32 nights of Magellan/IMACS and LDSS-2 (multi-slit), nine nights of MMT with Hectospec (multi-fiber) or Blue Channel (single slit), seven nights of CTIO-4 m/Hydra (multi-fiber), five nights of KPNO-4 m/MARS (multi-slit), and two nights of Gemini-N/GMOS (multi-slit) were used to obtain optical spectroscopy for our ChaMP sources. These spectra were supplemented with optical spectra from the SDSS DR6 archive. Among the 1569 spectra, 50% are broad-line AGNs (BLAGNs; FWHM > 1000 km s^{-1}), 16% narrow emission line galaxies (NELG; EW > 5 Å, FWHM < 1000 km s^{-1}), 14% absorption line galaxies (ALGs; no emission lines with EW > 5 Å), and 20% stars. Results from the stellar sample are published in Covey et al. (2008).

A table of our final extragalactic spectroscopic catalog is provided in electronic format. The catalog omits the 327 stars, and so contains a total of 1242 entries. The columns listed are as following.

CHANDRAOBSID: Chandra observation identifier;
SPECOBJID: spectroscopic observation identifier;
CXOMPNAME: ChaMP identifier;
R.A.: optical R.A. (*J*2000);
DECL.: optical DECL. (*J*2000);
TELESCOPE: telescope used for obtaining spectrum;
SPEC: spectrograph used for obtaining spectrum;
DATE: date of spectroscopic observation;
REDSHIFT: spectroscopic redshift;
CLASS: spectroscopic classification, BLAGN (broad-line AGN), NELG (narrow emission line galaxy), ALG (absorption line galaxy);
NETB: number of counts and associated errors;
FSC: soft (0.5–2 keV) X-ray flux in units of 10^{-13} erg s^{-1} cm^{-2} and associated errors;
FHC: hard (2–8 keV) X-ray flux in units of 10^{-13} erg s^{-1} cm^{-2} and associated errors;
FUV: far-UV AB magnitude and associated errors;
NUV: near-UV AB magnitude and associated errors;
U: *u*-band AB magnitude and associated errors;
G: *g*-band AB magnitude and associated errors;
R: *r*-band AB magnitude and associated errors;
I: *i*-band AB magnitude and associated errors;
Z: *z*-band AB magnitude and associated errors;
Y: *y*-band Vega magnitude and associated errors;
J: *J*-band Vega magnitude and associated errors;
H: *H*-band Vega magnitude and associated errors;
K: *K*-band Vega magnitude and associated errors;
MAG34: 3.4 μm Vega magnitude and associated errors;
MAG46: 4.6 μm Vega magnitude and associated errors;
MAG12: 12 μm Vega magnitude and associated errors;
MAG22: 22 μm Vega magnitude and associated errors;
S20: 20 cm radio flux in mJy and associated errors;
LOG LX: logarithmic 2–10 keV X-ray luminosity in units of erg s^{-1};
GAMMA: power-law slope from X-ray spectral fitting and associated 90% confidence;
NHINT, $N_{\rm H}^{\rm intr}$ and associated 90% confidence;

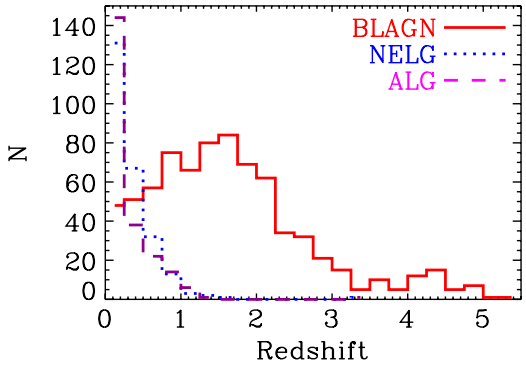

Figure 1. Redshift distribution for all 1242 spectroscopically identified ChaMP extragalactic sources.

(A color version of this figure is available in the online journal.)

NPHOT: number of photometric bands per catalogue used for the SED fitting (X: *Chandra*: G: *GALEX*, O: Optical, N: near-infrared, W: *WISE*, R: radio);

AGNTEMP: AGN template used for the SED fit (0: No AGN used, 1: Elvis et al. 1994 + Richards et al. 2006, 2: Hopkins et al. 2007, 3–6: Seyfert-2 from Bianchi et al. 2006, 7: NGC 1068 by Matt et al. 1997, 8: Mrk231 by Berta et al. 2006, 9: IRAS19254-7245 by Berta et al. 2003, 10: IRAS22491-1808 by Farrah et al. 2003;

GALTEMP: galaxy template used for the SED fit (0: No galaxy template used, 1: NGC 5253 by Beck et al. 1996, 2: NGC 7714 by Brandl et al. 2004, 3: M82 by Strickland et al. 2004, 4: IRAS12112+0305 by Imanishi et al. 2007, 5: Elliptical from Rowan-Robinson et al. 2008, 6: Young elliptical from Maraston 2005);

FSB: fraction of starburst contribution to the bolometric luminosity;

FA: fraction of AGNs contribution to the bolometric luminosity;

LBOL: bolometric luminosity (10^9–10^{19} Hz) in erg s^{-1};

MBH: logarithmic estimate of black hole mass.

Figures 1 and 2 show the redshift and multi-wavelength photometry distributions, respectively, of all our 1242 extragalactic sources. Our sample includes a significant population of 78 $z > 3$ X-ray QSOs, including two with redshifts greater than five. Figures 3–6 show examples of the various types of spectra found in our sample. Figure 7 shows the distribution of broadband X-ray flux versus optical magnitude to illustrate the parameter space spanned by the various populations. The majority of BLAGNs follow the trend of $0 < \log(f_X/f_r) < 1$. However, there is a significant population of BLAGNs that lie at $f_X/f_r > 10$. From the latter 30% of them appear to be X-ray Seyferts (10^{42} erg s^{-1} $< L_{2-10\,\mathrm{keV}} < 10^{44}$ erg s^{-1}) with $N_{\mathrm{H}}^{\mathrm{intr}} > 10^{22}$, which is consistent with previous studies that find that this parameter space is occupied by obscured X-ray Seyferts (e.g., Silverman et al. 2010). NELG seem to span a wide range of f_X/f_r as expected, as among them we can find Seyferts, LINERs, and star-forming sources. At faint flux levels, a significant number of ALGs are evident, spanning a wide range of optical magnitudes.

2.3. Multi-Wavelength Photometry

A prime advantage of ChaMP in comparison to deeper pencil-beam X-ray surveys is its relatively shallow depth that allows for easier source identification in other wavelengths. We have cross-correlated our spectroscopic sample with *GALEX* (Morrissey et al. 2007), UKIDSS DR4 (Lawrence et al. 2007), Two Micron All Sky Survey (2MASS; Skrutskie et al. 2006), Very Large Array (VLA; Condon et al. 1998), and *WISE* (Wright et al. 2010) catalogs. In the case of *GALEX*, the list was generated from a search for *GALEX* counterparts to optical counterpart positions in the ChaMP X-ray catalog. We retrieved the *GALEX* GR6 catalog using the virtual observatory (VO) TOPCAT tool (Taylor 2005). Using Monte Carlo simulations and the Fadda et al. (2002) method, we have concluded that a search radius of 2.5 arcsec provides us with a $P(d) < 0.02$, where $P(d)$ is the Poisson probability of a *GALEX* source to have a random association within a distance d, yielding an expected rate of random associations of less than 5%. The catalog contains only sources that were detected at S/N > 5 in at least one of the NUV, FUV filters. All matches were then visually inspected to remove any apparent spurious associations.

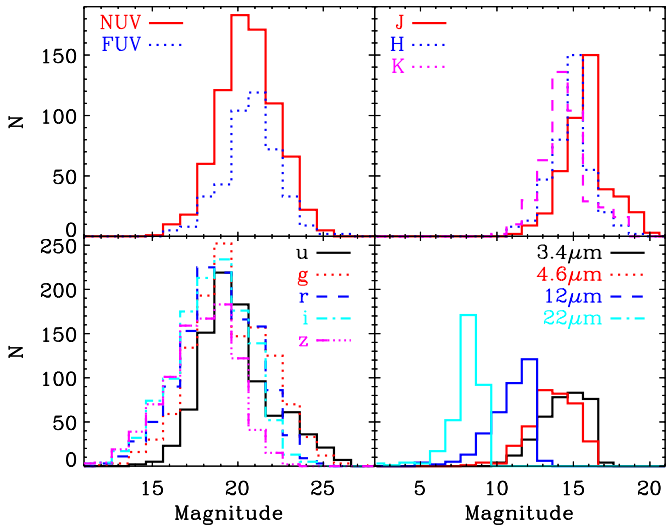

Figure 2. Multi-wavelength magnitude distributions for all our 1242 spectroscopically identified ChaMP extragalactic sources. UV and optical magnitudes are in the AB system, near- and mid-infrared magnitudes are in the Vega system.

(A color version of this figure is available in the online journal.)

We adopted a similar method for near-infrared with the 2MASS and UKIDSS (DR4) catalogs. The ChaMP team has also obtained deep near-infrared imaging for 35 fields using the ISPI camera on the CTIO 4 m Blanco telescope. We shifted the ChaMP source coordinates 6 arcmin in both R.A. and decl. in a large number of directions, performing positional cross-correlation with UKIDSS and 2MASS using a search radius of 5 arcsec. We thereby conclude that $P(d) < 0.02$, corresponding here to 4.5% random associations. In cases of multiple matches where one of the matches is at separation <1.5 arcsec and the other at separation >1.5 arcsec, the nearest match has been selected. In all other cases where matches are at similar distances, or both below 1.5 arcsec, visual inspection usually has broken the counterpart ambiguity. When both 2MASS and UKIDSS imaging are available, we use the deeper UKIDSS photometry for SED fitting (Section 3). The same method and statistics were used for *WISE* data.

In the case of NVSS and VLA-FIRST radio catalogs, a 5 arcsec match radius yields less than 2% random associations. All matches were visually inspected to remove any possible spurious associations. In the cases of FIRST/ChaMP associations where the radio/X-ray position is associated with an extended feature of the radio galaxy (e.g., radio lobe) the NVSS flux is used instead.

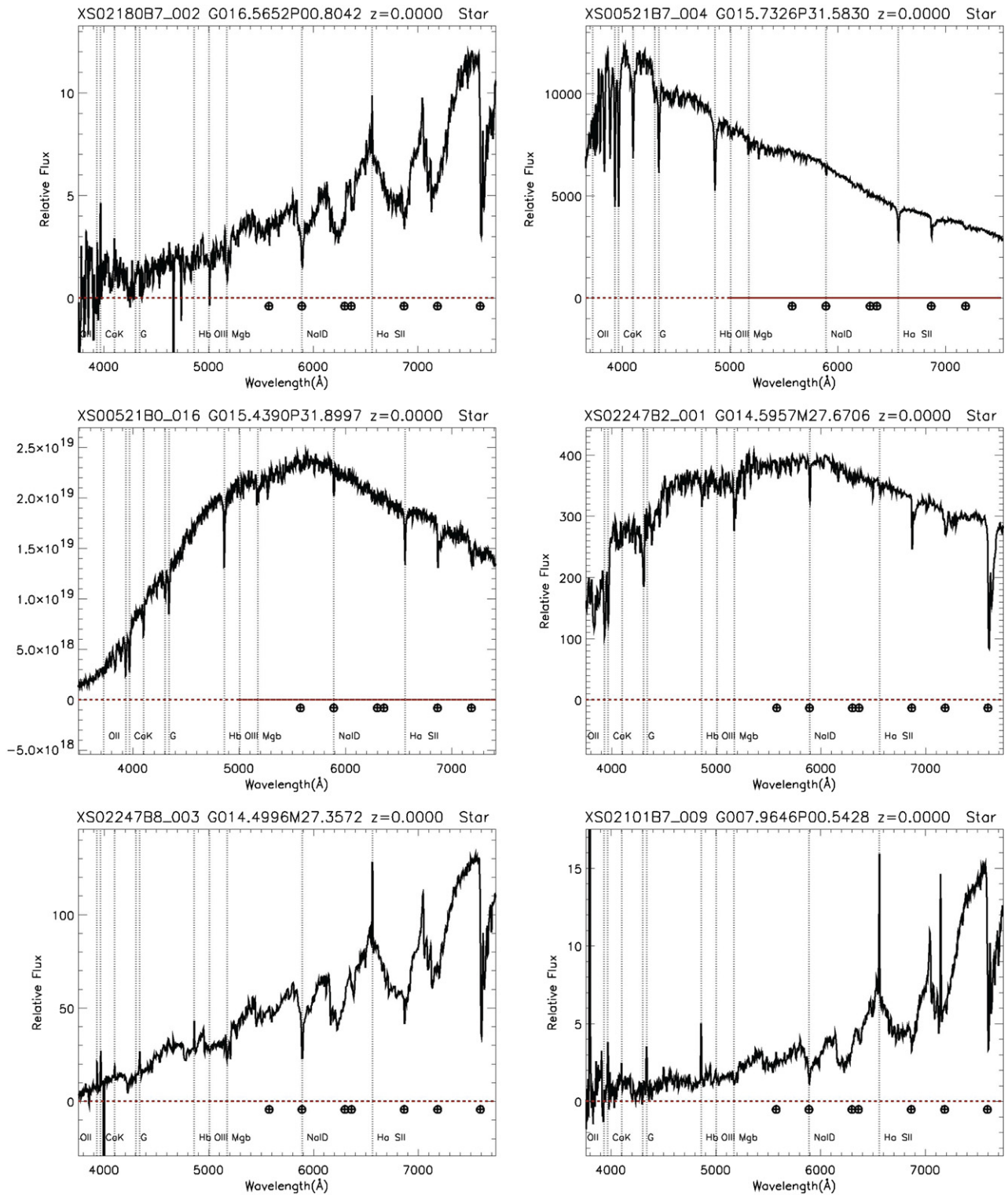

Figure 3. Example ChaMP spectra of stellar objects observed with FAST. CHANDRAOBSID, SPECOBJID, REDSHIFT, and CLASS are given on the top of each plot. (A color version of this figure is available in the online journal.)

From our 1242 ChaMP spectroscopic extragalactic sources, 63% have detections in UV, 100% in optical, 33% in near-infrared, 30% in mid-infrared, and 15% in radio.

3. BROADBAND SPECTRAL ENERGY DISTRIBUTIONS

To characterize the SEDs of extragalactic objects, estimate bolometric luminosities, and check for the presence of starburst and/or AGN activity in our sample, we fit the X-ray-to-radio fluxes with various empirical SEDs of well-observed sources as presented in Ruiz et al. (2010). We have used a total of 16 such templates: two QSO templates (Elvis et al. 1994 + Richards et al. 2006; Hopkins et al. 2007), four Seyfert-2 galaxies (Bianchi et al. 2006), four starburst galaxies (NGC 5253 by Beck et al. 1996; NGC 7714 by Brandl et al. 2004; M82 by Strickland et al. 2004; IRAS12112+0305 by Imanishi et al. 2007) with SFRs

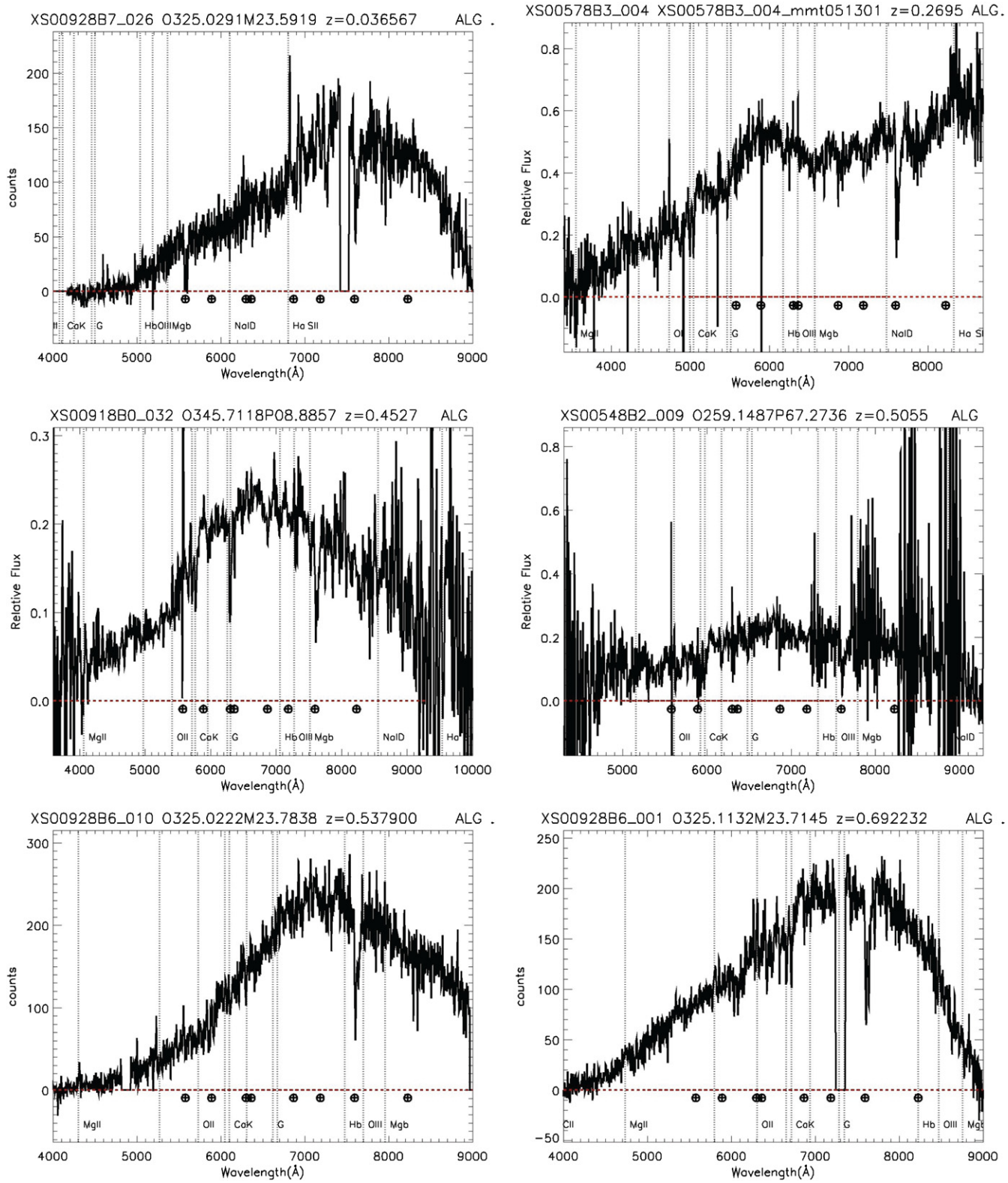

Figure 4. Example ChaMP spectra of absorption line galaxies observed with Magellan, MMT, and WIYN telescopes. Spectra are not flux calibrated. CHANDRAOBSID, SPECOBJID, REDSHIFT, and CLASS are given on the top of each plot.

(A color version of this figure is available in the online journal.)

ranging from 6 to 600 $M_{\odot}$ yr^{-1}, two absorption line galaxy templates (Rowan-Robinson et al. 2008; Maraston 2005), and four composite templates that are known to harbor both an AGN and a starburst (NGC 1068 by Matt et al. 1997; Mrk231 by Berta et al. 2006, 2007; IRAS19254-7245 by Berta et al. 2003; IRAS22491-1808 by Farrah et al. 2003). Except Mrk231 which is optically classified as a broad-line QSO with a massive young nuclear starburst, the remainder three composite objects are all optically classified as Seyfert-2s with intense starbursts. We have adopted the model described in Ruiz et al. (2010), which fits

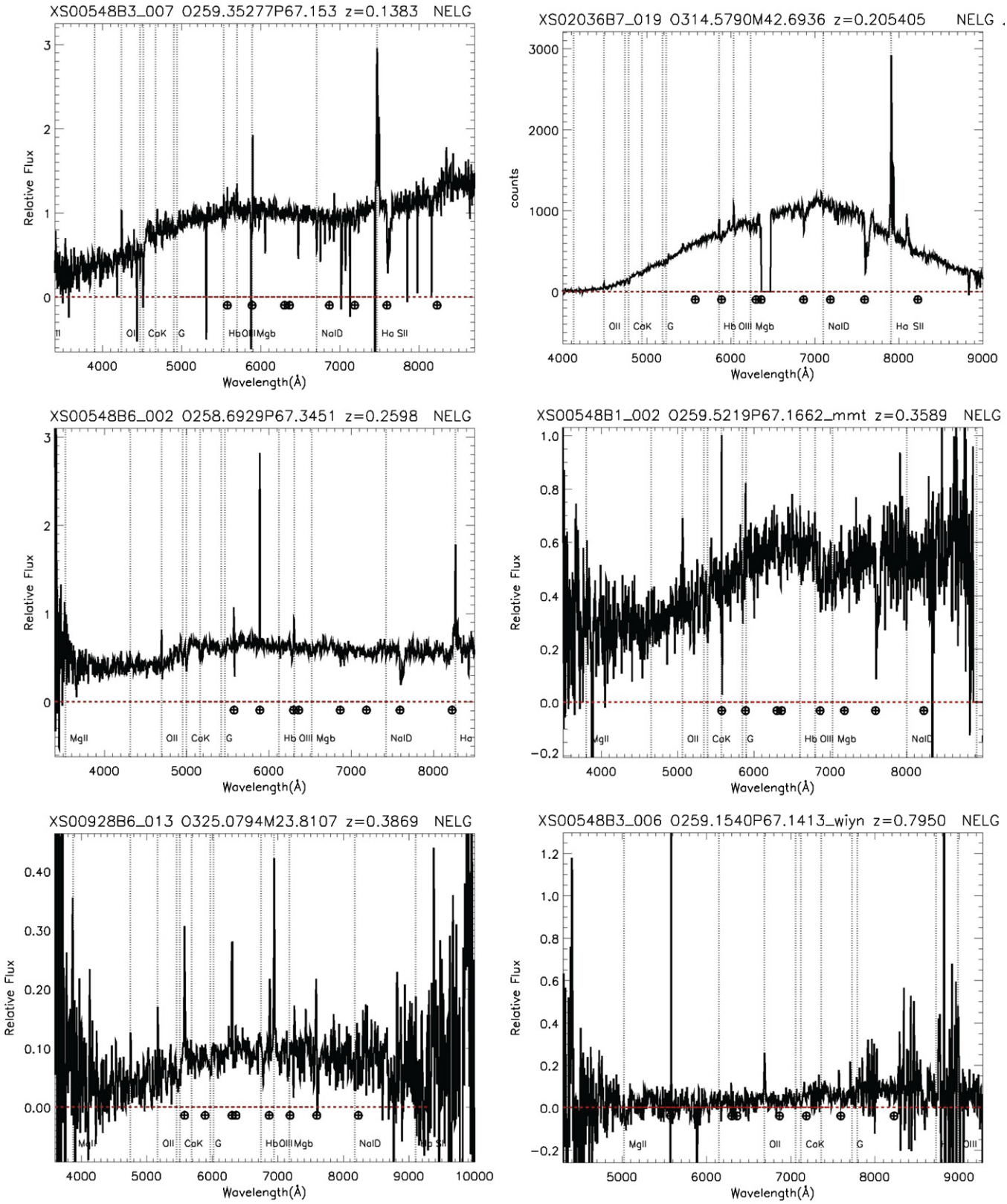

Figure 5. Example ChaMP spectra of narrow emission line galaxies observed with Magellan, MMT, and WIYN telescopes. Spectra are not flux calibrated. CHANDRAOBSID, SPECOBJID, REDSHIFT, and CLASS are given on the top of each plot.

(A color version of this figure is available in the online journal.)

all SEDs using a χ^2 minimization technique within the fitting tool Sherpa (Freeman et al. 2001). Our fitting allows for two additive components, one associated with the AGN emission and the other associated with the starburst emission. The SEDs are built and fitted in the rest frame. We have chosen the fit with the lowest reduced χ^2 as our best-fit model. Fractions of AGNs and starburst contributions are derived from the SED fitting normalizations, as these are derived from Ruiz et al. (2010)

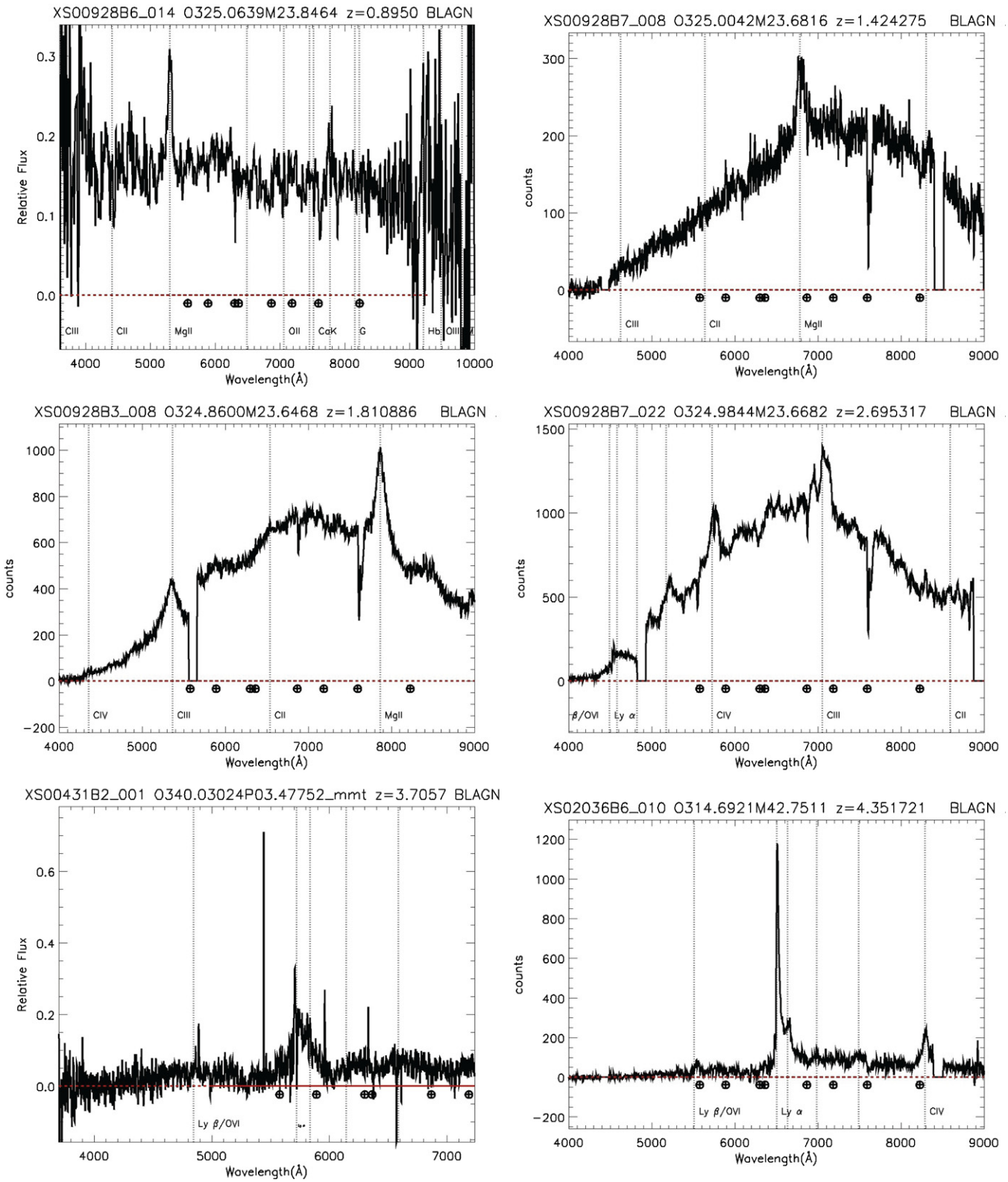

Figure 6. Example ChaMP spectra of broad-line AGNs observed with Magellan, MMT, and WIYN telescopes. Spectra are not flux calibrated. CHANDRAOBSID, SPECOBJID, REDSHIFT, and CLASS are given on the top of each plot.

(A color version of this figure is available in the online journal.)

model,

$$F_\nu = F_{\rm BOL}\left(\alpha u_\nu^{\rm AGN} + (1-\alpha)u_\nu^{\rm SB}\right), \quad (1)$$

where $F_{\rm BOL}$ is the total bolometric flux, α is the relative contribution of the AGN to $F_{\rm BOL}$, and F_ν is the total flux at frequency ν, while $u_\nu^{\rm AGN}$ and $u_\nu^{\rm SB}$ are the normalized AGNs and SB templates.

Among our 758 broad emission line objects (FWHM $>$ 1000 km s^{-1}) all are best fitted with one of our two available QSO SED templates, with 150 also requiring starburst

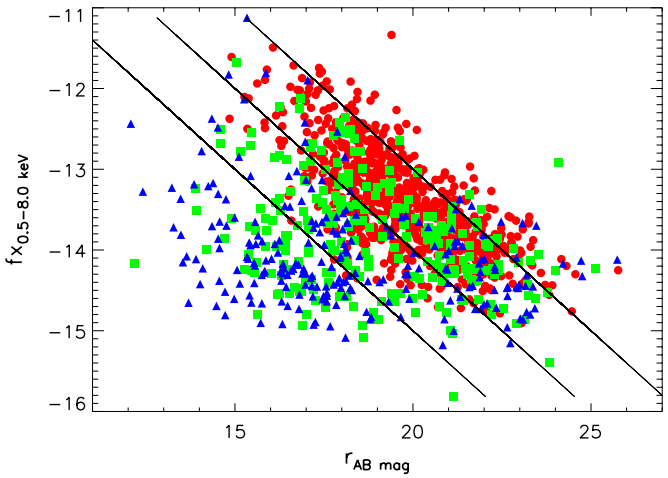

Figure 7. Broadband X-ray flux in logarithmic scale vs. *r*-band magnitude for all our 1242 extragalactic sources. Red circles, green squares, and blue triangles denote broad-line AGNs, narrow emission line, and absorption line galaxies, respectively. Line of constant X-ray-to-optical flux ratio (0.1, 1, 10) are given by Equation (1) of Szokoly et al. (2004).

(A color version of this figure is available in the online journal.)

contributions of at least 5%. Among the 252 narrow emission line objects (EW $>$ 5 Å; FWHM $<$ 1000 km s^{-1}), 17 have been fitted with one of the composite templates that harbor a Seyfert-2, 208 have been fitted with a Seyfert-2 template (65 having significant starburst contribution), 12 have been fitted with a starburst template, and 15 have been fitted with a QSO template (10 of which require $>$5% starburst contribution). Among the 230 absorption line galaxies, 130 have been fitted with an elliptical SED template, 91 with a mixture of Seyfert-2 and starburst templates, and nine objects with a QSO template. Since the best-fit model was determined only using the lowest reduced χ^2 value with no preselection based on spectroscopic classification, these results indicate an excellent overall agreement between the SED fitting code and optical spectroscopic classification in the cases of broad line and narrow emission line objects and fair agreement in the ALGs. Figure 8 shows examples of sources fitted with QSO, Seyfert-2, and composite templates.

4. X-RAY SPECTRAL FITTING

For all ChaMP X-ray sources in our spectroscopic sample, we perform X-ray spectral fitting using the CIAO *Sherpa*[18] tool in an automated script. For each source, we fit three power-law models. While quasars are typically well fit by a power law, it is well known that AGN-dominated spectra are complex, including potentially a soft excess and/or reflection component, Fe Kα line emission, and neutral, partially ionized, and/or partially covering absorption (e.g., Reeves & Turner 2000). When active SMBH accretion is weak or non-existent, emission related to the stellar component or interstellar medium (ISM) give rise to the X-ray emission in galaxies. X-ray spectra from lower luminosity objects may have a significant power-law component arising from X-ray binary populations (e.g., Persic & Rephaeli 2002; Fragos et al. 2009). Thermal components arising from hot ISM or shocked gas may be present, which at high signal-to-noise ratio (S/N) would be poorly fit with power-law models. However, since our sample has a median of 45 net broadband counts, detailed spectral fits are not warranted, so we remain content with power-law models.

The three X-ray spectral models we fit all contain an appropriate neutral Galactic absorption component frozen at the 21 cm value:[19] (1) photon index Γ, with no intrinsic absorption component (model "PL") and (2) an intrinsic absorber with neutral column $N_{\rm H}^{\rm intr}$ at the source redshift, with photon index frozen at $\Gamma = 1.8$ (model "PLfix"). Allowed fit ranges are $-1.5 < \Gamma < 3.5$ for PL and $10^{18} < N_{\rm H}^{\rm intr} < 10^{25}$ for PLfix. (3) A two-parameter absorbed power law where both Γ and the $N_{\rm H}^{\rm intr}$ are free to vary within the above ranges while $N_{\rm H}^{\rm Gal}$ is fixed (model "PL_abs"). All models are fit to the ungrouped data using Cash statistics (Cash, 1979). The latter model, PL_abs, is our default, for several reasons described below.

Overall, we find (Figure 9) that the best-fit Γ from our default model is not correlated with $N_{\rm H}^{\rm intr}$, which illustrates that these parameters are fit with relative independence even in low count sources. The best-fit Γ in the default PL_abs model correlates well with that from the PL model for the majority of sources; the median of the difference in fitted slopes for these two models $\Delta\Gamma$ is just 15% of the median uncertainty in slopes σ_Γ. On the other hand, 67 (5.4%) of sources have their best-fit power-law slope "pegged" at $\Gamma = 5$. Most (42% or 63%) of these are optical ALG, likely passive elliptical galaxies poorly fit by a power-law model. Only 10 (15%) are QSOs. Many of the sources with $\Delta\Gamma$ larger than σ_Γ also have detectable $N_{\rm H}^{\rm intr}$ (which we define as those fits where 90% confidence lower limit of $N_{\rm H}^{\rm intr} > 0$), which justifies the softer Γ result.

5. BLACK HOLE MASSES AND STAR FORMATION RATES

Black hole masses are only available for sources with available SDSS spectra. For our broad-line objects, black hole masses have been retrieved from Shen et al. (2011), who have compiled virial black hole mass estimates of all SDSS DR7 QSOs using Vestergaard & Peterson (2006) calibrations for Hβ and C IV and their own calibrations for Mg II. There are 329 broad-line objects within our sample with black hole mass estimates. For our narrow line objects, a total of 119 NELG for which high-quality SDSS spectra are available, $M_{\rm BH}$ values are calculated using the M–σ relation of Graham et al. (2011). A suite of optical and X-ray properties of these NELG are presented and discussed in Constantin et al. (2009).

SFRs have been estimated using the output of our SED fitting code. In the case that a starburst template is required in the fitting we extract the 8–1000 μm starburst luminosity which is a proxy for the far-infrared luminosity attributed to star formation. The $L_{\rm SB}$ (8–1000 μm) is then converted to a SFR using Kennicutt (1998) relation

$$\mathrm{SFR}(M_\odot\ \mathrm{yr}^{-1}) = 4.5 \times 10^{-44} \times L_{\rm SB}(\mathrm{erg\ s}^{-1}). \quad (2)$$

6. X-RAY LUMINOSITY–REDSHIFT PLANE

X-ray luminosity is by itself an important discriminator of the primary power source. The maximum achievable X-ray emission by young stellar populations in an ultraluminous starburst is $L_{2-10\,\rm keV} \sim 1.5 \times 10^{42}$ erg s^{-1} (Persic et al. 2004). Figure 10 shows the hard X-ray luminosity versus redshift for all hard X-ray detected sources in our sample. By restricting

[18] http://cxc.harvard.edu/sherpa

[19] Neutral Galactic column density $N_{\rm H}^{\rm Gal}$ taken from Dickey & Lockman (1990) for the *Chandra* aim point position on the sky.

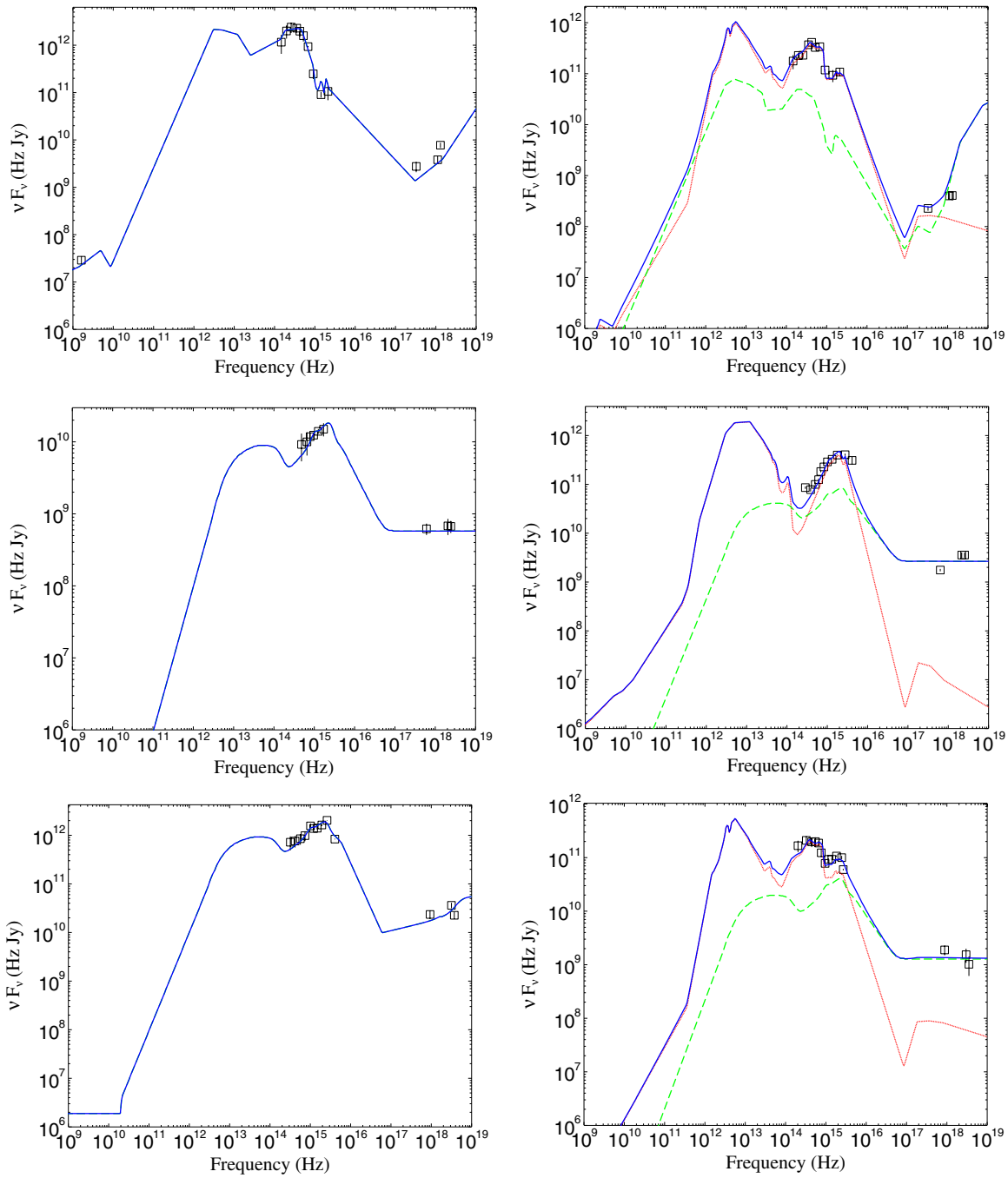

Figure 8. Examples of best-fit SEDs (blue line). Red solid and green dashed lines are the starburst and AGN templates, respectively. Square boxes indicate available photometry. Vertical lines are associated >10% errors. Top left: XS0518B7007 with $L_{2-10\,\mathrm{keV}} = 1.1 \times 10^{40}$ erg s^{-1} at $z = 0.08$. Best fitted with a Seyfert-2 NGC 3393 template. Top right: XS05618B6006 with $L_{2-10\,\mathrm{keV}} = 3.1 \times 10^{40}$ erg s^{-1} at $z = 0.08$. Best fitted with a Seyfert-2 NGC 4507 and a starburst NGC 7714 templates, contributing 15% and 85%, respectively, to the L_{BOL}. Middle left: XS00546B2012, with $L_{2-10\,\mathrm{keV}} = 9.1 \times 10^{43}$ erg s^{-1} at $z = 1.01$. Best fitted with an Elvis et al. (1994). QSO template. Middle right: XS02251B7002, with $L_{2-10\,\mathrm{keV}} = 9.5 \times 10^{43}$ erg s^{-1} at $z = 1.1$. Best fitted with an Elvis et al. QSO and a starburst NGC 5253 templates, contributing 15% and 85%, respectively, to the L_{BOL}. Bottom left: XS0907B3001 with $L_{2-10\,\mathrm{keV}} = 9.6 \times 10^{44}$ erg s^{-1} at $z = 2.08$. Best fitted with a Hopkins et al. (2007) QSO template. Bottom right: XS04151B6006 with $L_{2-10\,\mathrm{keV}} = 4.1 \times 10^{44}$ erg s^{-1} at $z = 1.92$. Best fitted with a Hopkins et al. QSO and a starburst NGC 7714 templates, contributing 20% and 80%, respectively, to the L_{BOL}.

(A color version of this figure is available in the online journal.)

the sample to those sources detected in the most penetrating 2–10 keV band we can minimize the influence of obscuration on our results. However, among our 1242 extragalactic ChaMP sources with available spectroscopy, 1202 have hard-band detections and as a result selecting them does not bias our results. Here, L_X is the rest-frame 2–10 keV X-ray luminosity calculated with the method described in the Appendix of Green et al. (2011). Red circles are those sources that require a starburst component to fit the observed photometry.

The L_X–z plane of Figure 10 shows a striking trend. Star formation occurrence increases from 43% in sources with log $L_{2-10\,\mathrm{keV}} < 42$ erg s^{-1} to 58% among objects with 42 erg s^{-1} < log $L_{2-10\,\mathrm{keV}} < 44$ erg s^{-1} and drops sharply to 26% when X-ray luminosity reaches QSO limits, i.e., when log

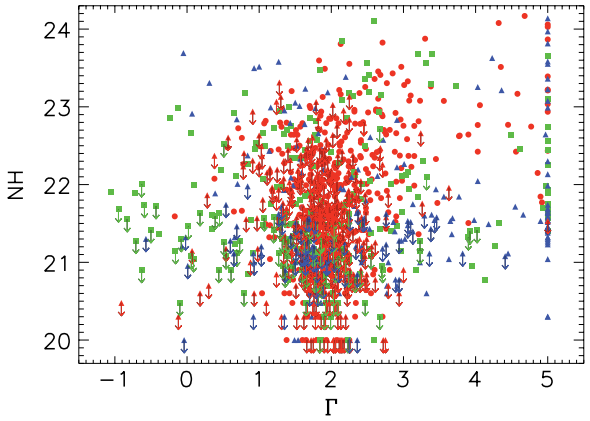

Figure 9. Best-fit X-ray spectral slope Γ vs. column density in logarithmic scale. Downward arrows represent the 90% upper limits to $N_{\rm H}^{\rm intr}$, whenever the 90% lower limit encompassed zero. Red circles, green squares, and blue triangles denote broad-line AGNs, narrow emission line, and absorption line galaxies, respectively.

(A color version of this figure is available in the online journal.)

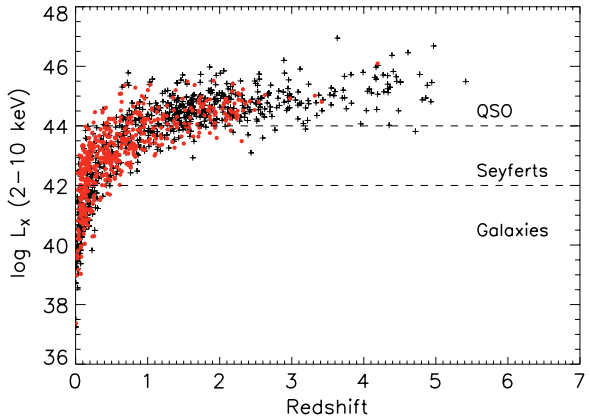

Figure 10. Distribution of rest-frame logarithmic 2–10 keV X-ray luminosity and spectroscopic redshift for the 1202 hard-band X-ray-detected sources from ChaMP. Red circles are sources that require a starburst component to fit available photometry. Black crosses are sources that their SED fits do not require any contribution from a starburst component. It is evident that as the X-ray luminosity increases, the occurrence of star formation activity decreases.

(A color version of this figure is available in the online journal.)

$L_{2-10\,\rm keV} > 44$ erg s^{-1}. However, the latter can be considered as a conservative upper limit to the occurrence of star formation in QSOs since the majority (69%) of X-ray QSOs with starburst events lie at $z > 1$ where contamination from torus emission to the mid-infrared can be significant (Rowan-Robinson et al. 2009; Mor & Netzer 2012). Since the longest infrared wavelength used for our SED fits is the 22 μm band from *WISE* we expect that the number of apparent star-forming QSOs at $z > 1$ may be significantly lower, which would make the trend we see in Figure 10 even stronger.

Figure 11 shows the average fractional contribution of AGNs and/or starburst components to the bolometric luminosity per 2–10 keV luminosity bin of 0.6. Again, there is a striking trend that seems to support the aforementioned indication of quenching of star formation in powerful QSOs. Although there seems to be a broad flat evolution of AGNs and starburst contributions in low and moderate X-ray luminosities ($L_X < 10^{41.5}$ erg s^{-1}), when powerful AGN activity is triggered ($L_X > 10^{42}$ erg s^{-1}), star formation seems to pick up and reaches its maximum at log $L_X \sim 42.5$. At this stage, AGNs and star formation appear to contribute the same fraction of the

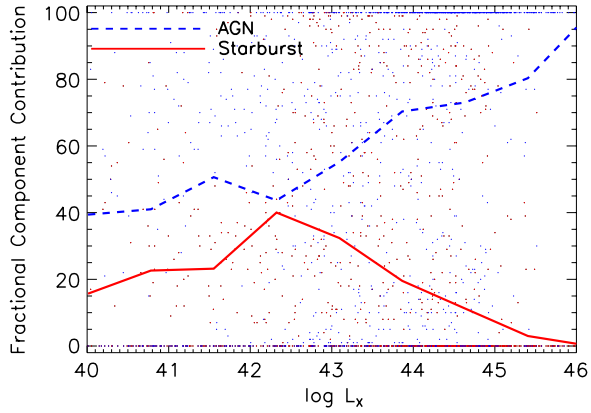

Figure 11. Fractional contribution of AGNs (blue dots) and starburst components (red dots) to bolometric luminosity vs. log L_X. Points represent the fractional AGNs and/or starburst contributions for all objects with $L_{X(2-10\,\rm keV} > 10^4$ erg s^{-1}. Solid red line represents the average value of starburst fractional contribution per log L_X bin of 0.6. Dashed blue line represents the average value of AGNs fractional contribution per log L_X bin of 0.6.

(A color version of this figure is available in the online journal.)

bolometric output but as the AGN becomes more powerful, as indicated both from the X-ray emission and AGNs contribution, star formation decreases rapidly and is eventually quenched when the AGN reaches extreme rates of accretion. At this stage of the evolution, AGN reaches its maximum emission (100% contribution from an AGN component) without the presence of any identifiable starburst events. This finding is consistent with the picture drawn by Figure 10. If the absence of star formation in QSOs, as depicted in Figure 10 were a detection bias, then we would expect that the QSOs with SFR to follow the relationship of Figure 11 and show enhanced starburst contribution compared with X-ray Seyferts. However, this is not the case, suggesting that intense SFR has stopped while accretion continues to rise in agreement with QSO-mode feedback models (e.g., Hopkins et al. 2005; Netzer 2009).

7. STARBURST DETECTABILITY

Figures 10 and 11 suggest that star formation is either quenched (weak or absent compared to the $L_{\rm BOL}$) in QSOs or simply not detectable by our SED fitting method using the currently available photometry. The latter may occur because a given host ($L_{\rm SB}$) falls below photometric survey detection limits toward higher redshift, and/or because a given host ($L_{\rm SB}$) becomes more difficult to detect in contrast to a more luminous nuclear source.

To address the detectability issue we have performed a series of SED fits to a large set of simulated sources drawn from our original sample. We have focused our tests to the population of 987 sources with $L_{X(2-10\,\rm keV)} > 10^{42}$ erg s^{-1}. Of them, 456 have 10^{42} erg s^{-1} $< L_{X(2-10\,\rm keV)} < 10^{44}$ erg s^{-1} (XSEY hereafter), and 531 have $L_{X(2-10\,\rm keV)} > 10^{44}$ erg s^{-1} (XQSO hereafter). To compare starbust detectability (i.e., completeness) between the predominantly lower redshift XSEY and the XQSOs, from the observed SEDs of sources that originally required at least 5% starburst contribution to their $L_{\rm BOL}$ (the "SF" sample hereafter), we first artificially remove the appropriately normalized fluxes of the best-fit starburst template from the observed photometric bands. The resulting "stripped" sample can then be treated identically in our detectability experiment as the "naked" sample—those sources whose observed SEDs were originally fitted with a pure AGN template. In this way, we can then add

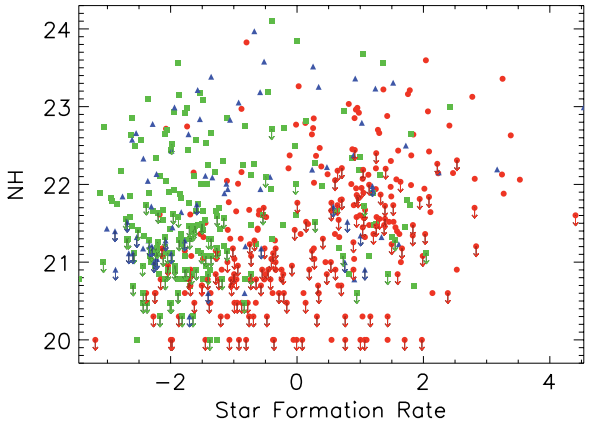

Figure 12. Star formation rates vs. column density in logarithmic scale. Downward arrows represent the 90% upper limits to $N_{\rm H}^{\rm intr}$, whenever the 90% lower limit encompassed zero. Red circles, green squares, and blue triangles denote broad-line AGNs, narrow emission line, and absorption line galaxies, respectively.

(A color version of this figure is available in the online journal.)

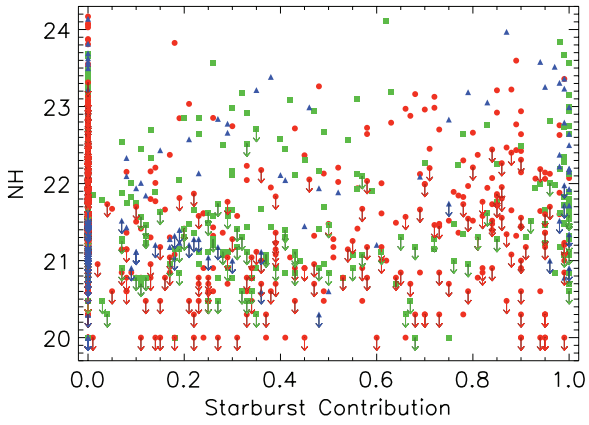

Figure 13. Percentage of starburst contribution to the bolometric luminosity vs. column density in logarithmic scale. Downward arrows represent the 90% upper limits to $N_{\rm H}^{\rm intr}$, whenever the 90% lower limit encompassed zero. Red circles, green squares, and blue triangles denote broad-line AGNs, narrow emission line, and absorption line galaxies, respectively.

(A color version of this figure is available in the online journal.)

back in a starburst component at various levels to the observed SEDs, and refit the simulated SEDs, to test the sensitivity of our method. 384 of 531 XQSOs are naked, and 176 of 456 XSEY are naked. Combining the "stripped" and the "naked" samples yields 987 pure AGN SEDs with no starburst contribution.

In the next step, for each of these 987 objects we fit a pure AGN template to estimate of its bolometric flux. Then, using each one of our four starburst templates, we compute an additional starburst component representing a fixed fraction of the total bolometric flux. The additional component ranges from 0% to 50% in intervals of 5%. We then interpolate the new starburst component at the frequency points of original SED, thus obtaining starburst fluxes. Finally, we add these simulated starburst fluxes to the "striped/naked" fluxes of the source. From each object/template pair, we thus create 11 new simulated SEDs, yielding $987 \times 4 \times 11 = 43{,}428$ simulated sources. We then run again our SED fitting code on all these simulated sources to constrain the starburst contribution. Of the XQSOs simulated with $\geqslant$5% SB, our best-fit SED that includes SB = 5% is $C_Q = 39\%$. By contrast, of all the XSEY simulated with $\geqslant$5% SB, our best fit that includes SB = 5% is $C_S = 52\%$ Thus, our completeness for XQSOs *relative* to XSEY is $R_C = C_Q/C_S = 39/52 = 0.75$. We can compensate crudely for this relative incompleteness by dividing our actual sample fraction of XQSO with SB $\geqslant$ 5% with R_C, $\mathrm{FSB_Q}/R_C$, which yields $26\%/0.75 = 35\%$ of XQSO. Since that fraction is still significantly lower than the actual fraction of XSEY with SB $\geqslant$ 5%, $\mathrm{FSB_S} = 58\%$, we can claim that the star formation in XQSOs appears significantly weaker from what we would expect if starburst luminosity increased with accretion luminosity.

8. THE RELATIONSHIP BETWEEN ABSORPTION AND STAR FORMATION

In previous studies, a connection has been made between X-ray absorption and star formation in AGNs (e.g., Page et al. 2004), though this remains controversial (e.g., Lutz et al. 2010; Shao et al. 2010). To test for whether any correlation exists between $N_{\rm H}^{\rm intr}$ and star formation in our sample, we must use statistical analysis that can account for upper limits. We examine log $N_{\rm H}^{\rm intr}$ versus log SFR and also versus starburst fraction FS for the 524 of our 1242 objects for which FS > 5%. When the 90% lower limit to $N_{\rm H}^{\rm intr}$ from our X-ray spectral fits is consistent with zero, we assign its 90% upper limit value as the upper limit for the correlation tests. We test for significance using the Cox Proportional Hazard, Kendall's τ, and Spearman's ρ tests, as implemented in the ASURV (Survival Analysis for Astronomy) package (Lavalley et al. 1992). Between log $N_{\rm H}^{\rm intr}$ and the log SFR, we find that the correlation is significant (i.e., the null hypothesis of no correlation is rejected) at the 0.1% level in the Spearman's ρ test. However, the Cox and Kendall's τ test show P 19% and 13%, respectively, which indicates no significant correlation. The lack of a significant relation with SFR is perhaps not so surprising; since SFR is essentially a luminosity, a strong distance effect is encoded therein, which may mask an intrinsic physical relationship.

When we test the correlation between log $N_{\rm H}^{\rm intr}$ and the star formation fraction FS (Figures 12 and 13), we find $P \leqslant 0.1$ for all three tests; the correlation is highly significant. The slope of the best-fit linear regression, however, is rather flat: $\mathrm{FS} = 0.0122 \pm 0.0016 \log N_{\rm H}^{\rm intr} + 19.84$ with a standard deviation of 0.724 from the Buckley–James algorithm.

There are a number of reasons why this treatment may not be ideal. First, we lump all source types together (BLAGNs, NELG, and ALG), which may be inappropriate for the actual physics in question. Second, there is no a priori reason why we should consider the logarithm of $N_{\rm H}^{\rm intr}$ versus FS, except that the distribution is more regular. Also, we exclude objects with FS < 5%, which could be treated similarly as upper limits. However, the number of limits would thereby greatly exceed the number of detections of a starburst component. These would be all piled up at FS = 0 and would strongly bias our regression fits. Perhaps more importantly, we note that our X-ray spectral fits do *not* include (nor in general have sufficient S/N to warrant) an emission model component appropriate to strong starburst activity. X-ray emission from star formation regions would generally be rather soft due to thermal emission, making the soft X-ray absorption features even more difficult to detect.

A more credible test may be to examine only the X-ray Seyferts, the subsample of objects with $10^{42}\,\mathrm{erg\,s^{-1}} < L_{2-10\,\mathrm{keV}} < 10^{44}$ erg s^{-1}. Although the obscuration of some AGNs is a consequence simply of the geometry of the surrounding material and our line of sight to the nucleus (Antonucci

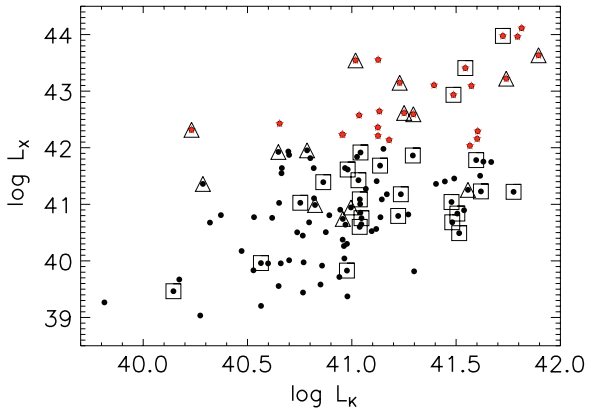

Figure 14. Rest-frame 2–10 keV logarithmic X-ray luminosity vs. logarithmic *K*-band luminosity for all ChaMP spectroscopically identified absorption line galaxies with *K*-band detections. Red stars are the population of 25 XBONGs, ALGs with $L_{X(2-10\,\mathrm{keV})} > 1.5 \times 10^{42}$ erg s^{-1}. Open triangles are radio-loud sources. Open squares are sources with log $N_{\mathrm{H}}^{\mathrm{intr}} > 22$.

(A color version of this figure is available in the online journal.)

1993), the prevalence of X-ray absorption in star-forming AGNs could imply an alternative source of absorbing material, perhaps related to the gas that is fueling the star formation or to outflowing material from the early stages of AGN feedback. In order to test this hypothesis we restrict our sample to the 430 X-ray Seyferts among which 273 objects have only upper limits to $N_{\mathrm{H}}^{\mathrm{intr}}$. First, we perform two-sample tests for a difference in log $N_{\mathrm{H}}^{\mathrm{intr}}$ between the 263 objects with FS $\geqslant 5\%$ (167 $N_{\mathrm{H}}^{\mathrm{intr}}$ limits), and the 167 with FS $< 5\%$ (106 $N_{\mathrm{H}}^{\mathrm{intr}}$ limits). The mean log $N_{\mathrm{H}}^{\mathrm{intr}}$ values are indistinguishable for the two subsamples at 21.0 ± 0.1, and their distributions using Wilcoxon and LogRank tests are also indistinguishable ($P > 88\%$). We also searched for correlations between star formation and absorption among only those 263 X-ray Seyferts with FS $> 5\%$, to avoid being dominated entirely by FS non-detections. Among this subsample, there are 96 detections of $N_{\mathrm{H}}^{\mathrm{intr}}$, but we find no evidence for a significant correlation either between log $N_{\mathrm{H}}^{\mathrm{intr}}$ and log SFR, or between log $N_{\mathrm{H}}^{\mathrm{intr}}$ and FS.

9. X-RAY BRIGHT OPTICALLY INACTIVE GALAXIES

Following the definition of an XBONG, ALGs with $L_{X(2-10\,\mathrm{keV})} > 1.5 \times 10^{42}$ erg s^{-1} (Comastri et al. 2002), we have identified a total of 81 XBONGs within our spectroscopic sample. However, as can be seen from Figure 7, a large number of ALGs appear to occupy the same parameter space as BLAGNs in the f_X/f_r plane. This might indicate the presence of AGN activity that has been missed due to the shallow optical spectroscopy. In order to address this issue we further restrict our sample by looking for XBONGs in the *K*-band-selected ALG sample. *K*-band detections come from UKIDSS DR4. We have identified a population of 25 XBONG within our *K*-band-selected sample in the redshift range $0.035 < z < 0.948$, 20% of the total *K*-band ALG-selected sample. Eleven of the sources appear to be associated with AGNs as their X-ray spectrum is described by a steep photon index that ranges between $1.4 < \Gamma < 1.9$. We find evidence for significant X-ray absorbing columns in seven of our sources—those that have $N_{\mathrm{H}} > 10^{22}$. Figure 14 shows the X-ray versus *K*-band luminosity of all the *K*-band-detected ALG sources within the ChaMP spectroscopic sample. Four possible explanations have been proposed for the nature of these objects (Green et al. 2004): a "buried" AGN (Comastri et al. 2002), a low-luminosity AGN (Severgnini et al. 2003), a BL Lac object (Yuan & Narayan 2004), and galactic scale obscuration (Rigby et al. 2006; Civano et al. 2007).

Green et al. (2004) defined a "buried" AGN as an object that has either no, or only narrow emission lines in its optical spectrum, strong evidence for $N_{\mathrm{H}} > 10^{22}$ in the rest frame and $L_{X(2-10\,\mathrm{keV})} > 10^{43}$ erg s^{-1} without absorption correction. Among our 22 objects there are four objects that fulfill all of the above criteria and are probably Type-2 QSOs. Our SED fitting suggests that only one of the objects is consistent with an elliptical like broadband spectrum. The remaining three are all fitted with a combination of a Type-2 Seyfert and a starburst template consistent with a "buried" AGN. In two of the latter, the starburst contribution dominates the bolometric emission at the 95% level. There are an additional six XBONGs in our sample that have $L_{X(2-10\,\mathrm{keV})} > 10^{43}$ erg s^{-1}, no signs of broad optical emission lines in their spectra, and soft X-ray spectra, which are most likely "buried" Type-2 AGNs. Our SED fitting has identified half of them as ellipticals, two as Type-1 QSOs with some <35% star formation contribution, and one Type-2 Seyfert with 10% star formation contribution. There are only two XBONGs in our sample that exhibit strong radio emission. Both of them have $L_{X(2-10\,\mathrm{keV})} > 10^{42}$ with $N_{\mathrm{H}} < 10^{21}$ and are fitted with an elliptical template with no evidence of star formation. These can both be BL Lac candidates but the lack of high S/N optical spectra that would allow us to measure the 4000 Å break does not permit us to verify their BL Lac status. All of the above suggest that the XBONGs found in our sample comprise a mixed bag of objects as suggested by Yan et al. (2011), primarily including normal elliptical galaxies, Type-1 AGN, and most importantly Type-2 QSOs that need further investigation.

10. HIGH-REDSHIFT X-RAY QSOs

There are a total of 78 $z > 3$ X-ray objects in our spectroscopic catalog, 70 from SDSS and eight from our own follow-up campaigns. The latter eight spectra are presented in Figure 15. Seventy-six are BLAGNs, one is a narrow emission line galaxy at $z = 3.417$, and one is an absorption line galaxy at $z = 3.32$. There are also two X-ray QSOs at $z > 5$ whose SDSS spectra are shown in Figure 16. All of our high-z sources have 0.5–2 keV detections and 76 have also 2–8 keV band detections. Seven sources have UV, all of them have *ugriz*, 18 have *JHK*, 22 have *WISE*, and 13 have radio detections. According to our SED fitting method, 76 are fitted with an Type-1 AGN template that in 22 cases requires a significant starburst contribution that ranges between 10% and 70% of the bolometric luminosity. The two non-broad-line high-redshift objects are both fitted with a starburst template, suggesting that these might be high-z Type-2 AGNs shrouded in a powerful starburst. The high-z sources in our sample have a relatively high number of detected counts, 31 is the median value, with respect to the depth of the X-ray observations. There are 15 sources that have more than 100 counts. In this count regime, we can assume that the extracted spectral fit results are reliable enough to be used for column density estimations. Forty-five of our sources have $N_{\mathrm{H}} > 22$ suggesting that these sources are obscured.

Our sample represents the largest spectroscopically selected sample of $z > 3$ X-ray sources and the second largest compared with samples with available photometric redshifts (Civano et al. 2011). Our sample has almost doubled the number of spectroscopically identified $z > 5$ X-ray QSOs by adding two more sources (Figure 16) to the three previously known at $z = 5.19$ (Barger et al. 2005), $z = 5.3$ (Civano et al. 2011), and

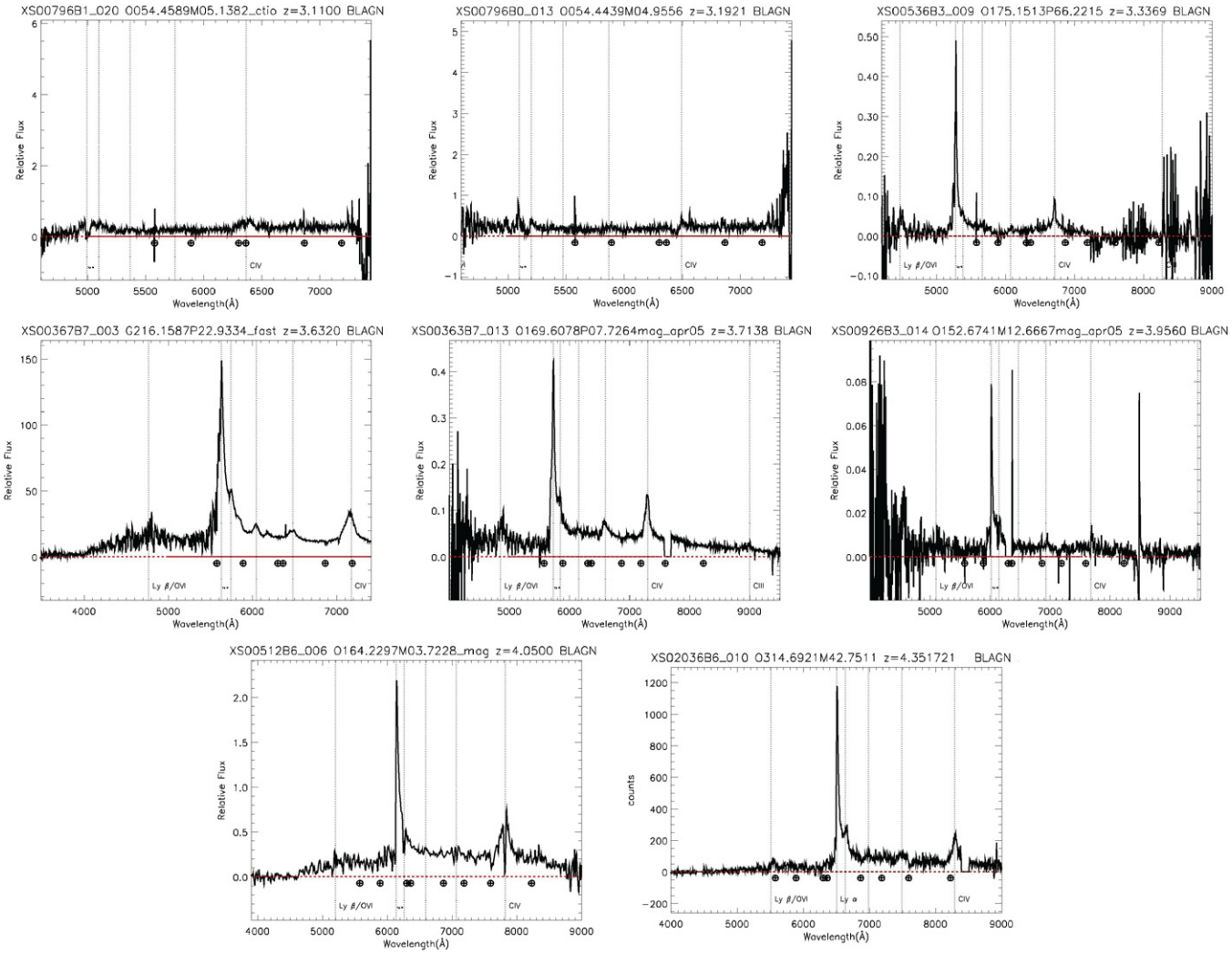

Figure 15. ChaMP $z > 3$ objects obtained using CTIO, FAST, WIYN, and Magellan telescopes. Spectra are not flux calibrated. CHANDRAOBSID, SPECOBJID, REDSHIFT, and CLASS are given on the top of each plot.

(A color version of this figure is available in the online journal.)

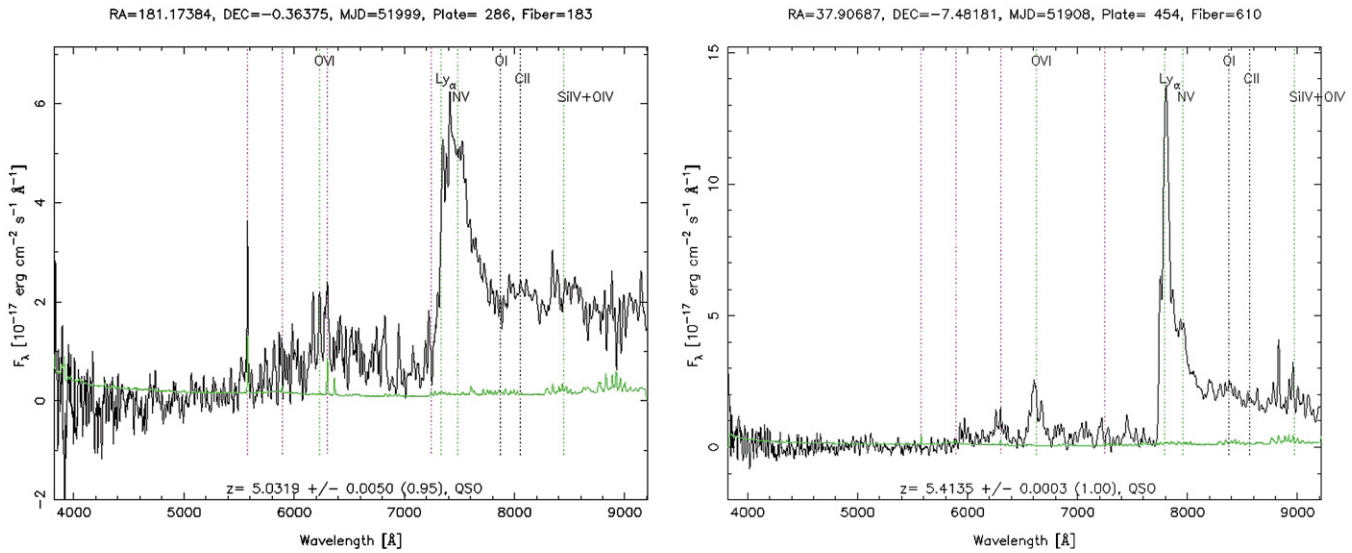

Figure 16. SDSS optical spectra of the two highest redshift objects found in our sample. They both are broad-line X-ray QSOs at $z > 5$.

(A color version of this figure is available in the online journal.)

$z = 5.4$ (Steffen et al. 2004). Here, we report the identification of the highest redshift X-ray QSO with optical spectroscopy ever found at $z = 5.4135$ (Figure 16).

11. CONCLUSIONS

We present the complete optical spectroscopic follow-up of ChaMP sources. We utilize a large suite of multi-slit and multi-fiber instruments on FLWO, SAAO, WIYN, CTIO, KPNO, MMT, Magellan, and Gemini to identify both bright and faint serendipitous X-ray sources as well as archival SDSS optical spectra. These observations resulted in a total of 1569 spectroscopic identifications of X-ray sources. Among the latter, there are 1242 extragalactic sources, half of which are broad-line QSOs. For these sources we have collected an extensive library of ancillary multi-wavelength data including X-ray, UV, optical, near-IR, mid-IR, and radio data from our own photometric follow-ups as well as various public catalogs including *GALEX*, 2MASS, UKIDSS, *WISE*, NVSS, and FIRST. Multi-wavelength photometry in combination with available optical spectroscopy has allowed us to distinguish among different populations, study the X-ray-to-radio SEDs in order to estimate luminosities and assess the level of AGNs and star formation contribution, estimate column densities via X-ray spectral fitting, and estimate black hole masses and SFRs.

Based on our observations, although X-ray Seyferts appear to be hosted in galaxies with powerful star formation events, when accretion onto the SMBH reaches its peak, as indicated from both hard X-ray luminosity and AGN contribution to the bolometric luminosity, star formation is quenched, resulting in only a small percentage of X-ray QSOs showing prevalent starburst events. According to Ebrero et al. (2009), objects with $L_{2-10\,\mathrm{keV}} \sim 10^{44}$ erg s^{-1} at $1 < z < 3$ are at the peak of their accretion rates. Therefore, the higher fraction of X-ray Seyferts with star formation compared with the X-ray QSOs with star formation, imply that the most prodigious episodes of star formation are common in the host galaxies of $1 < z < 3$ AGNs, but avoid powerful AGNs in which accretion is at its peak. This systematic separation of the peak periods of star formation and accretion implies a palpable interaction between the two processes, and provides a powerful discriminator for the form of AGN feedback that is responsible for terminating star formation in the host galaxy.

In "QSO-mode" feedback, a luminous AGN generates a powerful wind which terminates star formation by driving the ISM from the surrounding host galaxy. In "radio-mode" feedback, star formation is suppressed because collimated jets of relativistic particles emitted by a radiatively inefficient AGN prevent gas in the surrounding hot halo from cooling, thereby starving the galaxy of cool gas from which to form stars. Radio-mode feedback is commonly invoked in semianalytical models to limit galaxy masses and luminosities (Croton et al. 2006). In these models, black holes grow through luminous accretion episodes and black hole mergers. The correlation between black hole and bulge mass comes from assuming that a fixed fraction of the gas is accreted by the nucleus during each star-forming episode that results from a galaxy merger or disk instability, and hence star formation and accretion rate should be correlated over the full range of luminosity.

Our observations are therefore globally inconsistent with models such as Croton et al. (2006) in which AGNs influence their host galaxies only through radio-mode feedback. In contrast, models of galaxy formation in which quasar-mode feedback is responsible for terminating the star formation (Hopkins et al. 2006) predict that the AGN luminosity peaks later than the SFR, and thus are consistent with our observations that show that star formation not only occurs less often but is also weaker in X-ray QSOs compared with X-ray Seyferts. These models also predict that residual star formation, at the level of a few tens of percent of the peak, will continue during the period in which the AGN luminosity is at its maximum, consistent with our results, which show that some of the X-ray QSOs are still forming stars. Finally, while the observations presented here provide strong evidence for the violent quenching of star formation as AGNs reach peak luminosity, they do not rule out radio-mode feedback as the agent by which galaxy growth is subsequently suppressed. Further observations and/or studies with far-infrared/submillimeter data (Page et al. 2012) are essential in order to verify our last finding and to reduce any ambiguity based on template fitting results.

Our findings regarding the relationship between X-ray column density and starburst contribution and SFR further support the prediction that AGN obscuration is a consequence simply of the geometry of the surrounding material and our line of sight to the nucleus (Antonucci 1993) rather than a common material feeding both mechanisms. In this work, we have shown that obscuration does not seem to be associated to star formation either in the general population or the population of star-forming X-ray AGNs.

Finally, we report the identification of 25 *K*-band-selected XBONGs. Among the latter, 10 appear to be Type-2 QSOs with an AGN buried in active starburst events. We have also identified a significant population (78) of $z > 3$ objects. There are two non-broad-line objects in this sample that are quite probably high-z Type-2 AGNs. Forty-five of the high-z objects in our sample appear to be highly obscured. We finally report here the identification of two $z > 5$ X-ray QSOs who are among the highest spectroscopic redshift X-ray-selected QSOs ever observed.

The authors thank Francesca Civano and Hagai Netzer for their useful comments. Support for this work was provided by the National Aeronautics and Space Administration through *Chandra* Award nos. AR9-0020X and AR1-12016X, issued by the *Chandra* X-ray Observatory Center, which is operated by the Smithsonian Astrophysical Observatory for and on behalf of the National Aeronautics Space Administration under contract NAS8-03060.

REFERENCES

Aird, J., Nandra, K., Laird, E. S., et al. 2010, MNRAS, 401, 2531
Antonucci, R. 1993, ARA&A, 31, 473
Archibald, E., Dunlop, J. S., Jimenez, R., et al. 2002, MNRAS, 336, 353
Barger, A. J., Cowie, L. L., Mushotzky, R. F., et al. 2005, AJ, 129, 578
Beck, S., Turner, J. L., Ho, P. T. P., Lacy, J. H., & Kelly, D. M. 1996, ApJ, 457, 610
Berta, S., Fritz, J., Franceschini, A., Bressan, A., & Pernechele, C. 2003, A&A, 403, 119
Berta, S., Lonsdale, C. J., Siana, B., et al. 2007, A&A, 467, 565
Berta, S., Rubele, S., Franceschini, A., et al. 2006, A&A, 451, 881
Bianchi, S., Guainazzi, M., & Chiaberge, M. 2006, A&A, 448, 499
Brandl, B., Devost, D., Higdon, S. J. U., et al. 2004, ApJS, 154, 188
Brandt, W., Alexander, D. M., Hornschemeier, A. E., et al. 2001, AJ, 122, 2810
Cash, W. 1979, ApJ, 228, 939
Cen, R. 2011, ApJ, 741, 99
Civano, F., Brusa, M., Comastri, A., et al. 2011, ApJ, 741, 91
Civano, F., Elvis, M., Brusa, M., et al. 2012, ApJS, in press (arXiv:1205.5030)
Civano, F., Mignoli, M., Comastri, A., et al. 2007, A&A, 476, 1223
Comastri, A., Mignoli, M., Ciliegi, P., et al. 2002, ApJ, 571, 771
Condon, J., Cotton, W. D., Greisen, E. W., et al. 1998, AJ, 115, 1693

Constantin, A., Green, P., Aldcroft, T., et al. 2009, ApJ, 705, 1336
Cooper, M., Newman, J. A., Croton, D. J., et al. 2006, MNRAS, 370, 198
Covey, K. R., Agüeros, M. A., Green, P. J., et al. 2008, ApJS, 178, 339
Croton, D., Springel, V., White, S. D. M., et al. 2006, MNRAS, 365, 11
Di Matteo, T., Springel, V., & Hernquist, L. 2005, Nature, 433, 604
Dickey, J., & Lockman, F. J. 1990, ARA&A, 28, 215
Ebrero, J., Carrera, F. J., Page, M. J., et al. 2009, A&A, 493, 55
Elvis, M., Wilkes, B. J., McDowell, J. C., et al. 1994, ApJS, 95, 1
Fadda, D., Flores, H., Hasinger, G., et al. 2002, A&A, 383, 838
Farrah, D., Afonso, J., Efstathiou, A., et al. 2003, MNRAS, 343, 585
Fragos, T., Kalogera, V., Willems, B., et al. 2009, ApJ, 702, 143
Freeman, P., Doe, S., & Siemiginowska, A. 2001, Proc. SPIE, 4477, 76
Gilli, R., & Hasinger, G. 2001, A&A, 366, 407
Graham, A., Onken, C. A., Athanassoula, E., & Combes, F. 2011, MNRAS, 412, 2211
Green, P., Aldcroft, T. L., Richards, G. T., et al. 2009, ApJ, 690, 644
Green, P., Myers, A. D., Barkhouse, W. A., et al. 2011, ApJ, 743, 81
Green, P., Silverman, J. D., Cameron, R. A., et al. 2004, ApJS, 150, 43
Haggard, D., Green, P. J., Anderson, S. F., et al. 2010, ApJ, 723, 1447
Haines, C., Merluzzi, P., Mercurio, A., et al. 2006, MNRAS, 371, 55
Hasinger, G., Altieri, B., Arnaud, M., et al. 2001, A&A, 365, 45
Hasinger, G., Burg, R., Giacconi, R., et al. 1998, A&A, 329, 482
Hickox, R., & Markevitch, M. 2006, ApJ, 645, 95
Hopkins, A., & Beacom, J. 2006, ApJ, 651, 142
Hopkins, P., Hernquist, L., Cox, T. J., et al. 2005, ApJ, 630, 705
Hopkins, P., Hernquist, L., Cox, T. J., et al. 2006, ApJS, 163, 1
Hopkins, P., Richards, G. T., & Hernquist, L. 2007, ApJ, 654, 731
Hornschemeier, A., Brandt, W. N., Garmire, G. P., et al. 2001, ApJ, 554, 742
Imanishi, M., Dudley, C. C., Maiolino, R., et al. 2007, ApJS, 171, 72
Kalfountzou, E., Trichas, M., Rowan-Robinson, M., et al. 2011, MNRAS, 413, 249
Kauffmann, G., White, S. D. M., Heckman, T. M., et al. 2004, MNRAS, 353, 713
Kennicutt, R. 1998, ARA&A, 36, 189
Kim, M., Wilkes, B. J., Kim, D.-W., et al. 2007, ApJ, 659, 29
Lavalley, M., Isobe, T., & Feigelson, E. 1992, in ASP Conf. Ser. 25, Astronomical Data Analysis Software and Systems I, ed. D. M. Worrall, C. Biemesderfer, & J. Barnes (San Francisco, CA: ASP), 245
Lawrence, A., Warren, S. J., Almaini, O., et al. 2007, MNRAS, 379, 1599
Lehmer, B., Alexander, D. M., Chapman, S. C., et al. 2009, MNRAS, 400, 299
Lutz, D., Mainieri, V., Rafferty, D., et al. 2010, ApJ, 712, 1287
Magorrian, J., Tremaine, S., Richstone, D., et al. 1998, AJ, 115, 2285
Maraston, C. 2005, MNRAS, 362, 799
Matt, G., Guainazzi, M., Frontera, F., et al. 1997, A&A, 325, 13
Mor, R., & Netzer, H. 2012, MNRAS, 420, 526
Morrissey, P., Conrow, T., Barlow, T. A., et al. 2007, ApJS, 173, 682
Muller, G., Reed, R., Armandroff, T., Boroson, T. A., & Jacoby, G. H. 1998, Proc. SPIE, 3355, 577
Netzer, H. 2009, MNRAS, 399, 1907
Norman, D., & Impey, C. D. 2001, AJ, 121, 2392
Page, M., Stevens, J. A., Ivison, R. J., & Carrera, F. J. 2004, ApJ, 611, 85
Page, M., et al. 2012, Nature, in press
Persic, M., & Rephaeli, Y. 2002, A&A, 382, 843
Persic, M., Rephaeli, Y., Braito, V., et al. 2004, A&A, 419, 849
Reeves, J., & Turner, M. 2000, MNRAS, 316, 234
Richards, G., Strauss, M. A., Fan, X., et al. 2006, AJ, 131, 2766
Rigby, J., Rieke, G. H., Donley, J. L., Alonso-Herrero, A., & Pérez-Gonzlez, P. G. 2006, ApJ, 645, 115
Rosati, P., Tozzi, P., Giacconi, R., et al. 2002, ApJ, 566, 667
Rowan-Robinson, M., Babbedge, T., Oliver, S., et al. 2008, MNRAS, 386, 697
Rowan-Robinson, M., Valtchanov, I., & Nandra, K. 2009, MNRAS, 397, 1326
Ruiz, A., Miniutti, G., Panessa, F., & Carrera, F. J. 2010, A&A, 515, 99
Schawinski, K., Lintott, C. J., Thomas, D., et al. 2009, ApJ, 690, 1672
Severgnini, P., Caccianiga, A., Braito, V., et al. 2003, A&A, 406, 483
Shao, L., Lutz, D., Nordon, R., et al. 2010, A&A, 518, 26
Shen, Y., Richards, G. T., Strauss, M. A., et al. 2011, ApJS, 194, 45
Silverman, J., Mainieri, V., Salvato, M., et al. 2010, ApJS, 191, 124
Skrutskie, M., Cutri, R. M., Stiening, R., et al. 2006, AJ, 131, 1163
Steffen, A., Barger, A. J., Capak, P., et al. 2004, AJ, 128, 1483
Stern, D., Moran, E. C., Coil, A. L., et al. 2002, ApJ, 568, 71
Strickland, D., Heckman, T. M., Colbert, E. J. M., Hoopes, C. G., & Weaver, K. A. 2004, ApJS, 151, 193
Szokoly, G., Bergeron, J., Hasinger, G., et al. 2004, ApJS, 155, 271
Taylor, M. 2005, in ASP Conf. Ser. 347, Astronomical Data Analysis Software and Systems XIV, ed. P. Shopbell, M. Britton, & R. Ebert (San Francisco, CA: ASP), 29
Tozzi, P., Rosati, P., Nonino, M., et al. 2001, ApJ, 562, 42
Trichas, M., Georgakakis, A., Rowan-Robinson, M., et al. 2009, MNRAS, 399, 663
Trichas, M., Rowan-Robinson, M., Georgakakis, A., et al. 2010, MNRAS, 405, 2243
Vestergaard, M., & Peterson, B. 2006, ApJ, 641, 689
Worsley, M., Fabian, A. C., Bauer, F. E., et al. 2006, MNRAS, 368, 1753
Wright, E., Eisenhardt, P. R. M., Mainzer, A. K., et al. 2010, AJ, 140, 1868
Yan, R., Ho, L. C., Newman, J. A., et al. 2011, ApJ, 728, 38
Yuan, F., & Narayan, R. 2004, ApJ, 612, 724